ORIGINAL PAPER

CrossMark

STEM tomography of high-pressure frozen and freeze-substituted cells: a comparison of image stacks obtained at 200 kV or 300 kV

Paul Walther[1] · Andrea Bauer[1] · Nadia Wenske[1] · Alberto Catanese[2] · Débora Garrido[2] · Marion Schneider[3]

Abstract

Scanning transmission electron microscopic (STEM) tomography of high-pressure frozen, freeze-substituted semi-thin sections is one of multiple approaches for three-dimensional recording and visualization of electron microscopic samples. Compared to regular TEM tomography thicker sample sections can be investigated since chromatic aberration due to inelastic scattering is not a limit. The method is ideal to investigate subcellular compartments or organelles such as synapses, mitochondria, or microtubule arrangements. STEM tomography fills the gap between single-particle electron cryo-tomography, and methods that allow investigations of large volumes, such as serial block-face SEM and FIB-SEM. In this article, we discuss technical challenges of the approach and show some applications in cell biology. It is ideal to use a 300-kV electron microscope with a very small convergence angle of the primary beam ("parallel" beam). These instruments are expensive and tomography is rather time consuming, and therefore, access to such a high-end microscope might be difficult. In this article, we demonstrate examples of successful STEM tomography in biology using a more standard 200-kV microscope equipped with a field emission tip.

Keywords STEM tomography · Cell biology · Synapse · Electron microscopy · High pressure freezing · Freeze substitution

Introduction

Three-dimensional electron microscopic imaging provides fascinating new insights into cells and helps to increase our understanding of structure and function. For this purpose a high number of different electron microscopic sample preparation and imaging methods have been developed. With cryo-TEM single-particle tomography, the method that has been awarded the Nobel prize in chemistry 2017, even atomic resolution of proteins can be achieved under certain conditions. In the current communication, we discuss

✉ Paul Walther
  paul.walther@uni-ulm.de

1   Central Facility for Electron Microscopy, Ulm University, Albert-Einstein-Allee 11, 89081 Ulm, Germany

2   Institute of Anatomy and Cell Biology, Ulm University, Ulm, Germany

3   Division of Experimental Anesthesiology, University Hospital Ulm, Ulm, Germany

scanning transmission electron microscopic (STEM) tomography of biological samples, a method for three-dimensional reconstruction of relatively large portions of cells (typically about $3 \times 3 \times 0.7$ μm), however not with atomic resolution, but with "macromolecular resolution" of a few nanometers. This serves to study interactions at the level of cytoskeletal elements, vesicles, organelles and viral particles.

The principle of STEM tomography is similar to TEM tomography. A tilt series of images (typically from about $-72°$ to $+72°$ with $1.5°$ increment) is recorded from an area of interest. From these data the three-dimensional tomogram is calculated with a radon-transformation (Hoppe et al. 1974).

In contrast to TEM, the sample is not directly imaged in the STEM mode but is rather scanned by a focused electron beam with a diameter of less than 1 nm. After interaction with the sample, electrons are collected either directly below the sample, to measure the electrons that did not scatter to wide angles (bright-field mode) or are collected with a ring-like detector that collects the scattered electrons (dark-field mode). The image is formed line by line on a TV or computer screen. In biology, STEM has already been used for elemental analysis by measuring X-rays from the area of electron beam impact (e.g., Zierold and Steinbrecht 1987) and for mass measurements using the dark-field mode (e.g.,

Müller and Engel 2001). The crucial advantage of STEM tomography is that it allows for imaging of relatively thick sections up to 1 µm. In TEM tomography, section thickness is limited by chromatic aberration caused by inelastic scattering of the primary beam in the sample. By definition, inelastic scattering causes energy loss of the scattered primary electrons, leading to chromatic aberration in the lenses below the sample causing a blurred image. This effect increases with sample thickness, since the probability for an electron to be inelastically scattered increases with increasing thickness of the sample. In STEM tomography, there are no image forming lenses behind the sample, therefore, the inelastically scattered electrons cannot cause chromatic aberration but contribute to contrast formation. Therefore, compared to TEM tomography, thicker samples up to 1 µm can be analyzed (Yakushevska et al. 2007; Aoyama et al. 2008; Hohmann-Marriott et al. 2009; Höhn et al. 2011).

The most important condition for successful tomography in life science is, however, a well prepared sample. Due to the conditions in the electron microscope it needs to be solid state and 1 µm thick or less. Therefore, the 50–80% water in a biological sample needs either to be frozen (for cryo-TEM) or to be replaced by a polymer. All samples in this paper have been prepared by the later approach (polymer embedding) using high-pressure freezing of the cells under defined physiological conditions, and freeze substitution.

STEM tomography has found a number of applications in life science research and the following list is far from being complete. In a recent article McBride et al. (2018) investigated the blood platelet canalicular system with STEM tomography and compared the data with block-face SEM. The conclusion is that better resolution was obtained with STEM tomography. Hochapfel et al. (2018) investigated the *Drosophila* nephrocyte with STEM tomography to better understand the complex architecture of the nephrocyte channel system.

In our laboratory we have used STEM tomography of high-pressure frozen samples for the following applications. Secondary envelopment and release of human cytomegalovirus has been investigated by Walther et al. (2010) and Schauflinger et al. (2011, 2013). The process of secondary envelopment is especially suitable for STEM tomography, since the budding of the capsids into a membrane fits nicely into a section with a thickness of about 500 nm. The structure of mitochondria has been reexamined by Höhn et al. (2011). We thereby confirmed the cristae junction model, originally proposed by Daems and Wisse (1966), as well as a very close apposition of inner and outer mitochondrial membranes in a metabolically active mitochondrion as already suggested by Knoll and Brdiczka (1983). We have published three-dimensional Golgi stacks of HeLa cells in Giehl et al. (2011). Nafeey et al. studied structure of intermediate filamental networks using STEM tomography by and found that branching of intermediate filaments is fundamentally different from

actin filament branching (Nafeey et al. 2016). The endocytic uptake of nanodiamond–nanogold particles has been investigated with STEM tomography by Liu et al. (2016). Bragg-scattering caused a flickering effect in the nanodiamonds when looking at the tilt series which turned out as an interesting side-effect by tomographic acquisition. Thus nanoparticle tracking in cells was not restricted to nanogold but could be extended to the application of nanodiamonds. Kollmer et al. (2016) and Han et al. (2017) successfully investigated amyloid fiber networks in contact with cells. Moreover, the structure of the marine algae *Emiliania huxleyi* has been investigated by Yin et al. (2018) using STEM tomography. In a recent work we investigated the structure of synapses in nutrient deprived cell cultures (Catanese et al. 2018).

In this article we compare STEM tomography data obtained with two different electron microscopes, a high-end Titan 300-80 (http://thermofisher.com) and a more conventional JEOL 2100F (http://JEOL.com). In addition, we report several cell biological systems where STEM tomography is useful.

Materials and methods

Specimen preparation

Specimen preparation was performed according to the protocol of Villinger et al. (2014) All cultivated cells shown in the figures were grown on carbon coated sapphire discs with a diameter of 3 mm and a thickness of 160 µm (Engineering Office M. Wohlwend GmbH, Sennwald, Switzerland). Two sapphire discs were clamped with a 50 µm thick gold ring (diameter 3.05 mm, central bore 2 mm; Plano GmbH, Wetzlar, Germany) in between. The sapphire discs were oriented with the cells inward, so that the cells are protected in a small liquid chamber. This sandwich was then frozen in a Wohlwend HPF Compact 01 high-pressure freezer (Engineering Office M. Wohlwend GmbH, Sennwald, Switzerland). No prefixation was used, so that the cells were frozen from a defined physiological state. Care was taken that the sandwich is perfectly clamped by the holder to prevent liquid nitrogen to enter into the sandwich during high-pressure freezing.

Freeze substitution was performed as described in Walther and Ziegler (2002) with a substitution medium consisting of acetone with 0.2% osmium tetroxide, 0.1% uranyl acetate and 5% of water for good contrast of the membranes. During 17 h, the temperature was exponentially raised from −90 °C to 0 °C. After substitution, the samples were kept at room temperature for 1 h and then washed twice with acetone. After stepwise embedding of the samples in Epon, polymerization occurred at 60 °C for 72 h.

Thick sections of 700 nm to 1 µm were cut off from the epoxy resin block parallel to the plane of the sapphire disc with an Ultracut UCT ultramicrotome (Leica) equipped with

a 35° diamond knife (http://diatomeknives.com). Before mounting the slice onto a copper grid with parallel bars, the grid was plasma-cleaned with an Edwards plasma cleaning system. Afterwards, a droplet of 10% (w/v) poly-L-lysine (Sigma Aldrich) in water was added on the sample and dried for 5 min at 37 °C. The grid with the slice on it was treated on both sites with 15 µl of a solution containing 25 nm gold particles (http://aurion.com) diluted 1:1 with water. The gold particles serve as fiducial markers for image stack alignment. Finally, the grid was coated on both sites with a 5 nm carbon

layer using a BAF 300 electron beam evaporation device (http://opticsbalzers.com).

STEM tomography

Images were recorded in the STEM mode either with a Titan 300-80 (Thermo Fisher) at 300 kV accelerating voltage (Figs. 1, 2, 4a, b) or with a JEOL JEM-2100F (all other figures) at 200 kV.
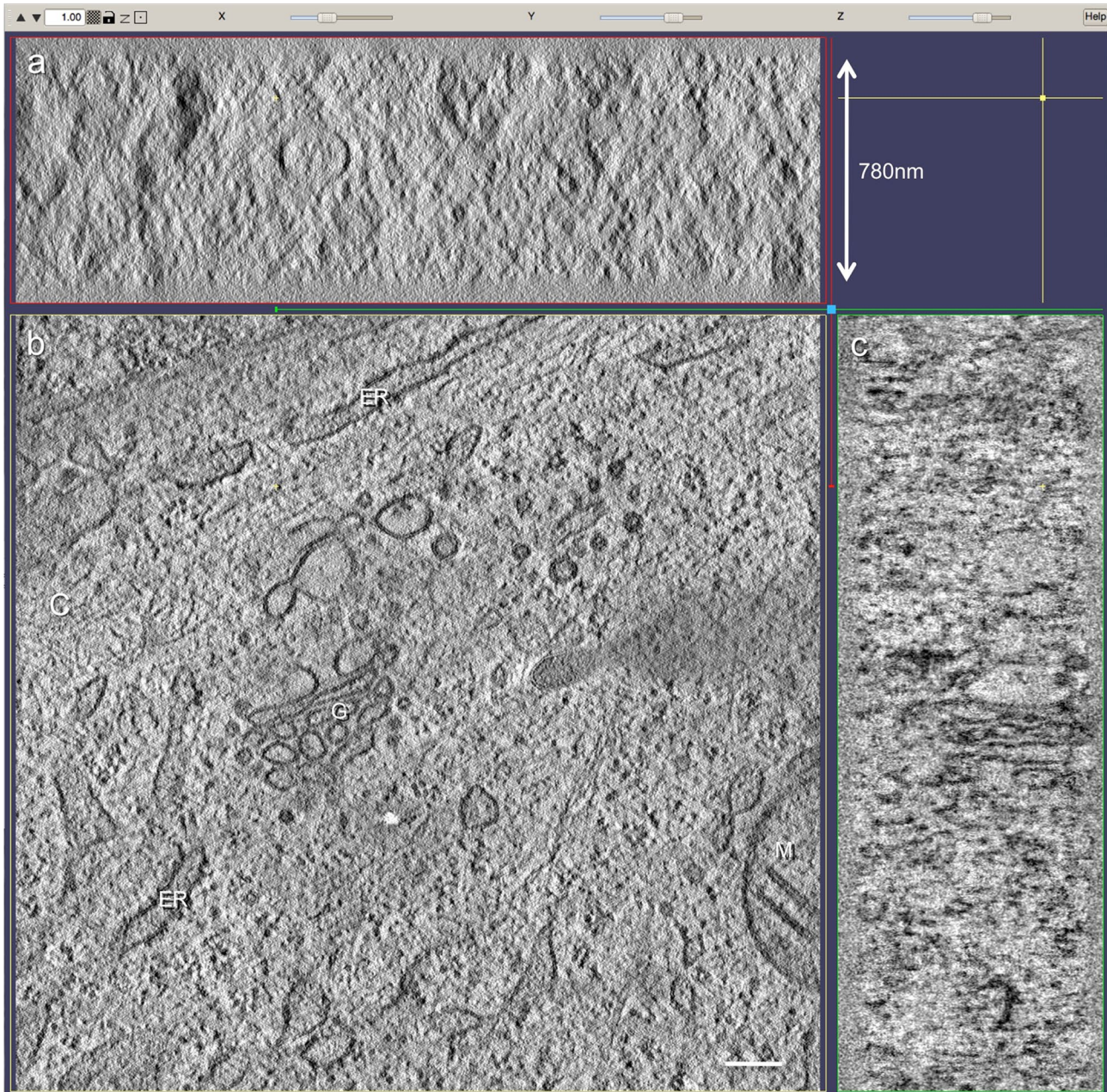

Fig. 1 STEM tomogram of a Bon cell's cytoplasm recorded with 300 kV acceleration voltage. The thickness of the section measured in the microscope is 780 nm. No obvious blurring of the structures along the Z-axis can be observed. **a** A virtual section in the XZ-plane, **b** in the XY-plane, and **c** in the YZ-plane. G Golgi apparatus, ER endoplasmic reticulum, M mitochondrion; bar 200 nm
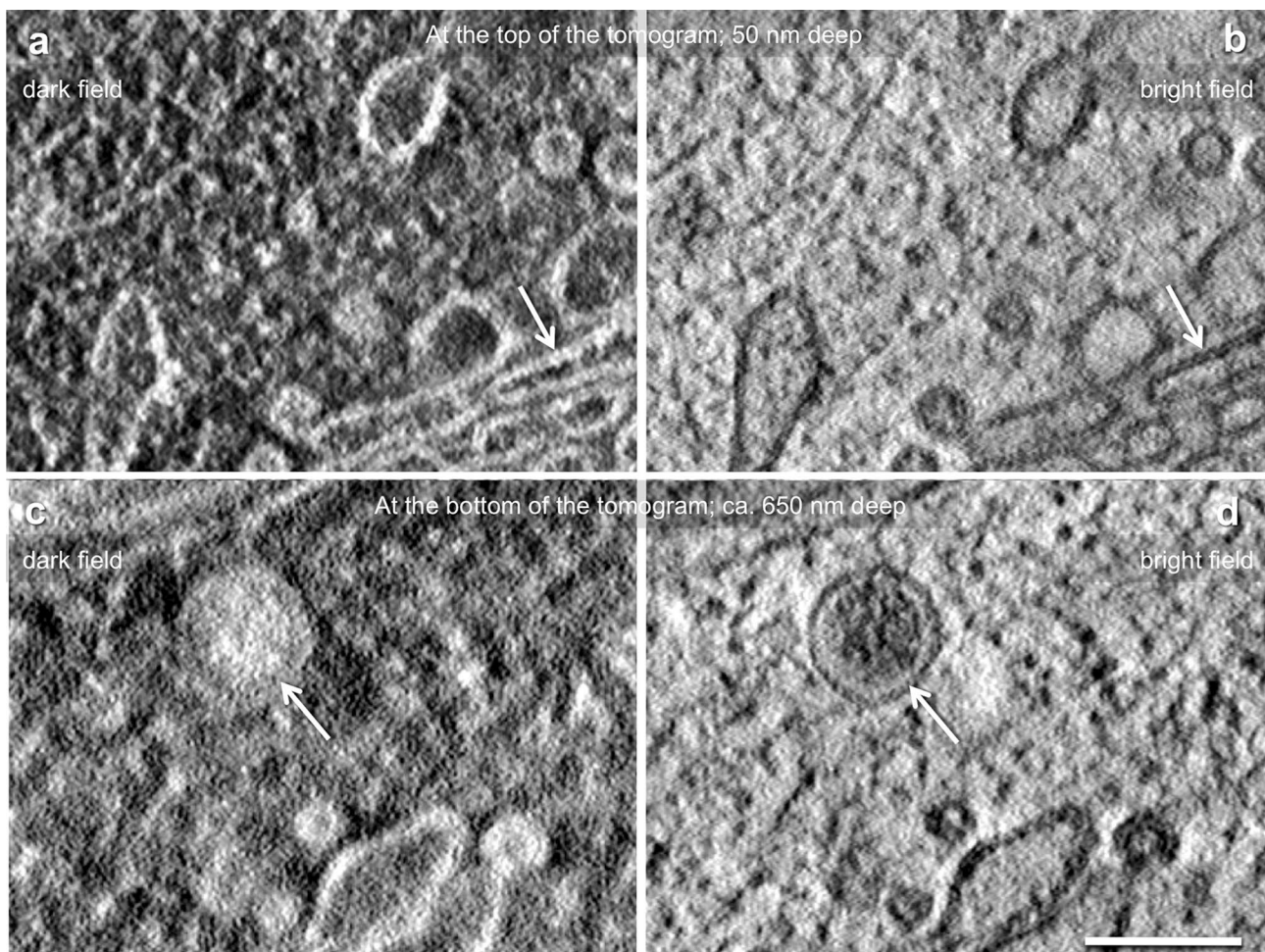
Fig. 2 Virtual sections of the Bon cell's tomogram of Fig. 1, at the top of the tomogram (50 nm deep; **a, b**) and at the bottom (ca. 650 nm deep; **c, d**). The dark-field image is sharp at the top (**a**), but slightly blurred at the bottom (**c**). The bright-field image, however, remains sharp through the whole tomogram (**b, d**); bar 200 nm

The settings of the microscopes were as follows.

Titan Accelerating voltage 300 kV, STEM mode; tilt angles $-72°$ to $+72°$, 1° increment.

Imaging mode: bright field or dark field with an annular dark-field detector (Fischione, Export, PA, USA) with a camera length of 301 mm. Illumination time per image was 18 s.

The semi-convergence angle was only 0.58 mrad due to the "parallel" beam alignment (Biskupek et al. 2010).

The tilt series were recorded with the software Xplore 3D (Thermo Fisher) each image had 1024×1024 pixels, pixel size was 2.62 nm, 145 images were used for a tomogram.

JEOL 2100F Accelerating voltage 200 kV, STEM mode; tilt angles $-72°$ to $+72°$, 1.5° increment.

Imaging mode: bright field with the JEOL bright-field detector. Illumination time per image was 22 s.

The semi-convergence angle was estimated to be about 5 mrad.

The tilt series were recorded with the software EM-Tools (TVIPS, Tietz) each image had 1024×1024 pixels, pixel size was 2.74 nm, 97 images were used for a tomogram.

Tomogram reconstruction was done with the IMOD software package vs. 4.7 and the programs Etomo and 3dmod (Kremer et al. 1996). To generate a 3D model of the individual images, the images were first aligned and subsequently reconstructed using the WBP (weighted back-projection) algorithm, except for Fig. 6b, which was obtained with the SIRT (simultaneous iterative reconstruction technique) algorithm with four iterations. Figure 6c, d was obtained by overlaying the images obtained with WBP and SIRT. The program Etomo was used with the presets, except for the window "Fine Alignment" where under "Global Variables" and "Distortion Solution Type" the option "Full solution" was activated (according to suggestions by Reinhard Rachel). In addition, in the window "Tomogram Generation" the option "take logarithm with the densities of" was activated and set
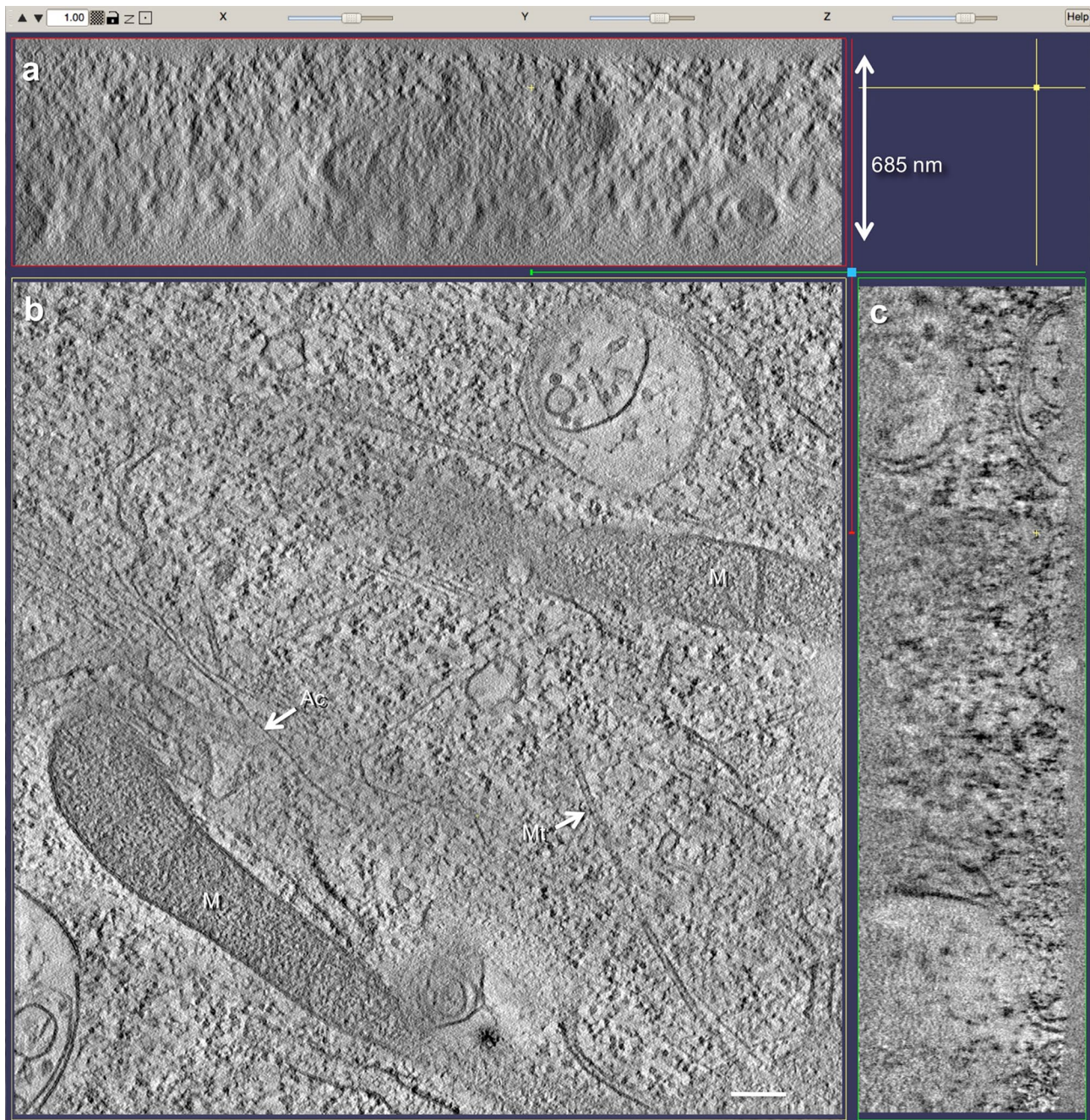
Fig. 3 STEM tomogram of a human glioblastoma cell's cytoplasm recorded with 200 kV acceleration voltage. The thickness of the section measured in the microscope is 685 nm. **a** A virtual section in the *XZ*-plane, **b** in the *XY*-plane, and **c** in the *YZ*-plane. Along the *Z*-plane the images from *XZ*- and *YZ*-plane become slightly blurred, *Ac* actin filament, *Mt* microtubule, *M* mitochondrion; bar 200 nm

to 32,768 (according to suggestion by David Mastronarde on the IMOD list).

The segmentations were either done with 3dmode from the IMOD package vs. 4.7 for Figs. 5 and 8, or with the software Avizo vs. 9.5 (http://thermofisher.com) for Figs. 6 and 7.

Results

Tomography data obtained with a Titan 300-kV (Thermo Fisher) instrument (Figs. 1, 2, 4b, d) and a 2100F from JEOL (all other figures) are compared. The section for the tomogram of Fig. 1 was cut with a setting of 1 µm at the microtome. The measured thickness of the section in the
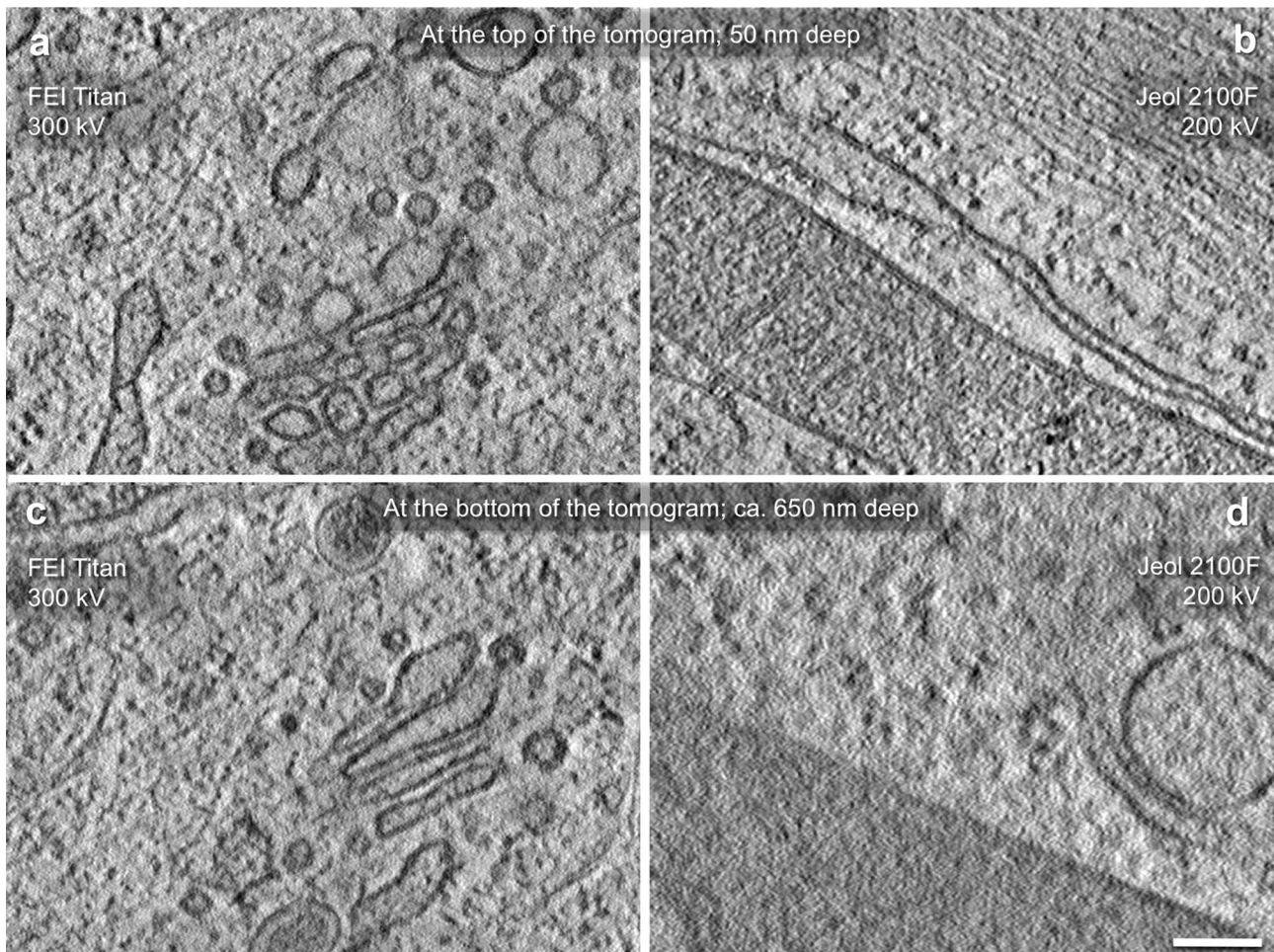
Fig. 4 Virtual sections from the tomograms in Fig. 1 (**a, c**) recorded at 300 kV, and from the tomogram in Fig. 3 (**b, d**) recorded at 200 kV. At the top both tomograms look very sharp, at the bottom, however, the virtual section of the 300-kV tomogram looks sharp (**c**), whereas the virtual section of the 200-kV tomogram is blurred (**d**); bar 200 nm

reconstruction (obtained from data recorded with the Titan), however, was 780 nm. Such a shrinkage of roughly 15–25% between the setting of the ultramicrotome and the measured thickness in the electron microscope was observed in all tomograms shown in this article. When observing the *YZ*-plane (Fig. 1a) or the *XZ*-plane (Fig. 1c) no difference in the sharpness of the structures along the *Z*-axis can be observed. The ultrastructure of the cultivated Bon cell is well preserved as can be seen in the virtual section of the *XY*-plane (Fig. 1b) showing endoplasmic reticulum (ER), a Golgi apparatus (G), portion of a mitochondrion (M) and a densely packed cytosol with numerous globular and filamentous elements indicating that during specimen preparation the first step high-pressure freezing did work well, without major ice crystal-related damage.

Figure 2 shows small areas of virtual sections from the tomogram of Fig. 1. Figure 2a, b shows dark-field and bright-field images of virtual sections at the top of the tomogram in a depth of roughly 50 nm. The images are of similar quality, the two leaflets of the lipid bilayer are nicely resolved in both images (arrows). In virtual sections from the bottom of the tomogram (Fig. 2c, d), however, structures such as lipid bilayers are blurred in the dark field image (arrow in Fig. 2c), but still reasonably sharp in the bright-field image (Fig. 2d). This effect has been described by Hohmann-Marriott et al. (2009) and it is confirmed in all our tomograms recorded with the Titan and with the JEOL 2100F microscope. Therefore, all the following images shown in this article are from data recorded with the bright-field detector.

The purpose of this article is to investigate whether STEM tomography can also be done with a more affordable microscope than Thermo-Fisher-Scientific's high-end 300-kV Titan. Therefore, we used a JEOL 2100F to record the tomograms. The difference of major impact is the accelerating voltage which is only 200 kV. Another difference is the convergence angle of the primary beam. A larger
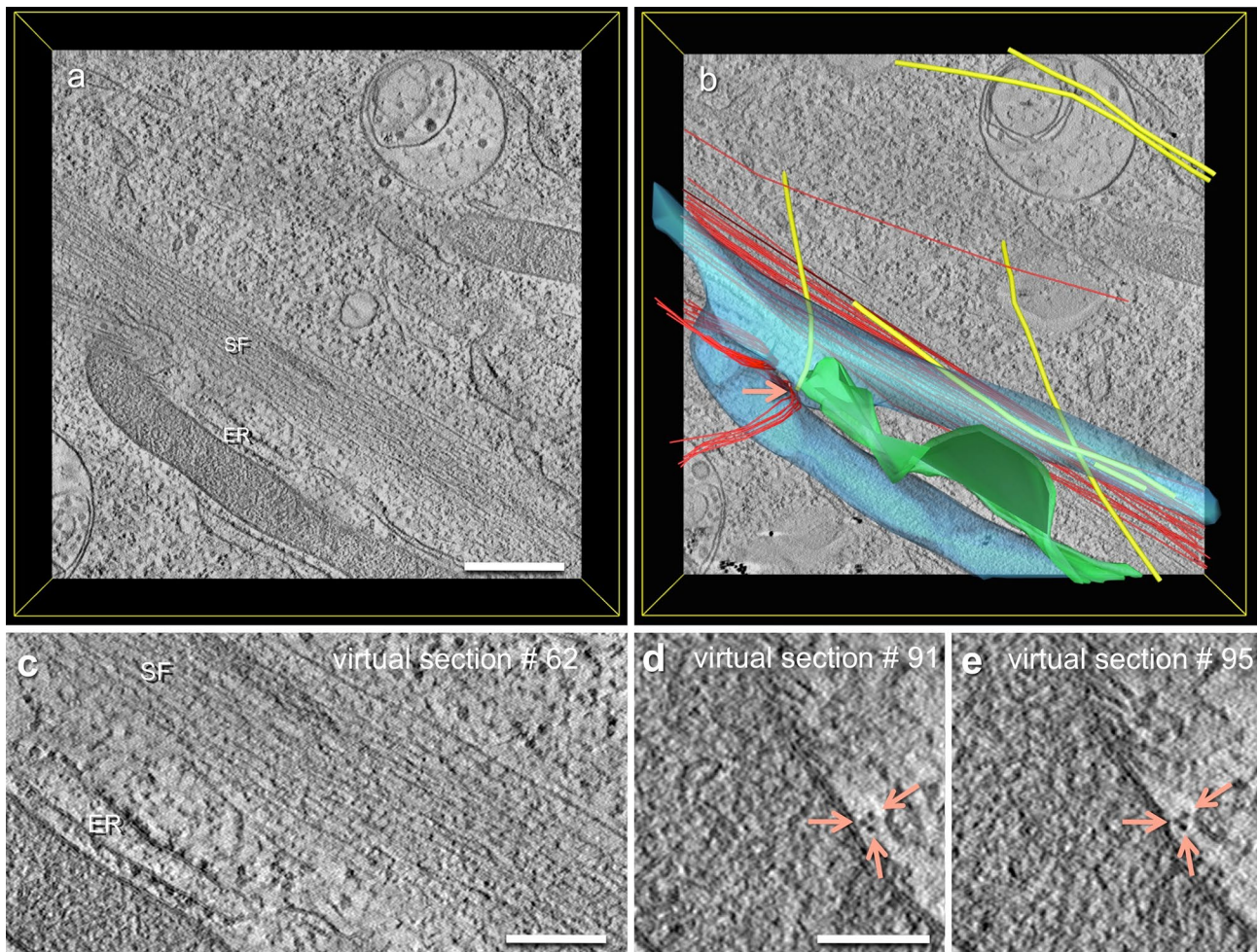
Fig. 5 Segmentation of the tomogram of a human glioblastoma cell shown in Fig. 3. **a** shows a calculated virtual section. In **b** some structures are segmented, namely actin filaments (red), a branching mitochondrion (blue), some microtubules (yellow) and a portion of the endo- plasmic reticulum, in part dilated by tumor-specific ER-stress (green); bar 500 nm. **c** A higher magnification of virtual section 62 showing a stress fiber consisting of actin filaments; bar 250 nm. In **d**, **e** cross sections of three actin filaments are labeled with the red arrows; bar 100 nm

convergence angle leads to a poorer depth of focus. Figure 3 is a tomogram from a portion of a cultivated human glioblastoma cell with a thickness of 685 nm, as measured in the electron microscope. The first striking difference to the 300-kV Titan tomogram of Fig. 1 is the decreasing sharpness of the tomogram in Z that can be observed when looking at the virtual sections of the YZ-plane (Fig. 3a) and the XZ-plane (Fig. 3c). The virtual section in the XY-plane is from close to the upper surface of the section and it shows clearly and well-resolved structural details of the cells such as microtubules (Mt), actin filaments (Ac), mitochondria (M).

Figure 4 shows portions of virtual sections of the tomograms in Fig. 1 (Titan; 300 kV) and Fig. 3 (JEOL 200 kV). At the top of the tomograms (Fig. 4a, b) both virtual sections look sharp and the membrane bilayers are well resolved. In virtual sections of the bottom of the tomogram, however, the tomogram obtained with the Titan 300 kV (Fig. 4c) is

much sharper than the tomogram recorded with the 200 kV JEOL (Fig. 4d). So, to summarize Figs. 1, 2, 3 and 4, best results were achieved with the 300-kV Titan with collecting the bright-field images. The tomograms recorded with the JEOL 200 kV are of excellent quality at the top of the section, but became slightly blurred toward the bottom of a 685-nm-thick section. Because of the better accessibility, the data of all following figures were collected with the 200-kV JEOL 2100F.

The tomogram of a glioblastoma cell (Fig. 3) is further analyzed in Fig. 5. One striking structure is the stress fiber bundle formed by actin filaments that crosses through the whole width of the tomogram (Fig. 5a). Some but not all of the actin filaments are segmented in red in Fig. 5b and further magnified in Fig. 5c. Some of the actin filaments are bent around an arm of the Y-shaped mitochondrion as can be seen in the segmentation in Fig. 5b (here again, not all actin filaments

have been segmented). The red arrow depicts actin filaments running perpendicularly to the virtual section plane. This area is shown at a higher magnification in Fig. 5d (section 91) and 5E (section 95). The arrows depict three cross sections of such actin filaments. This demonstrates the remarkably good resolution of our approach. The three-dimensional organization becomes especially well visible in the movie to Fig. 5 that is added to the Supplementary Material.

We usually do reconstruction of the tilt series with the weighted back-projection (WBP) protocol of IMOD vs. 4.7 (Kremer et al. 1996). The software also has the option to use the simultaneous iterative reconstruction technique, (SIRT). It uses considerably more computer power which is probably a reason that it has not been used so widely in biology. Figure 6a shows a portion of a virtual section after reconstruction with WBP and Fig. 6b after reconstruction with SIRT. After WBP small structural details were very well visible, however, gray-scale differences at a larger scale were better preserved with SIRT. Therefore we mixed both signals (Fig. 6c) which improves the overall visual aspect of the virtual sections. This method was applied for the reconstruction of a glioblastoma cell's cytoplasm (Fig. 6d). It is impressive to see how densely packed a cell is, even though, only a small amount of the cytoplasm is actually segmented in this tomogram. The movie to Fig. 6 (Supplementary Material) compares WBP and SIRT and the merged signal and helps to obtain an idea of the three-dimensional arrangement of the cellular components.

Stem tomography of high-pressure frozen macrophages enables us to reevaluate intracellular endocytotic trafficking routes. Many samples display a rather different appearance when cryo-fixed and imaged in three dimensions. Figure 7 is a tomogram from a human M2, so-called anti-inflammatory macrophage. In the three-dimensional reconstruction of Fig. 7, an extended tubular network becomes visible as described in Bauer et al. (2017). Figure 7 gives a detailed view into the different tubular structures. In this tomogram we can distinguish three different kinds of tubules: (1) large empty tubules colored blue in the segmentation and labeled with blue arrows in the higher magnification of virtual section 92 (Fig. 7d); (2) tubules densely filled, also containing membranes and membrane fragments, colored in green and labeled with green arrows in Fig. 7d; (3) chain-like tubules with variable diameters are labeled yellow. All these tubules are surrounded by one lipid bilayer only and, thereby, can be unambiguously discerned from mitochondria.

Figure 8 shows a synapse from cultivated neuronal rat cells as described by Catanese et al. (2018). Highlighted are the (1) presynaptic part, (2) the synaptic vesicles, (3) the postsynaptic part and (4) the postsynaptic density area. A total of $n = 774$ synaptic vesicles have been segmented in this tomogram and this becomes very well visible in the movie to Fig. 8.
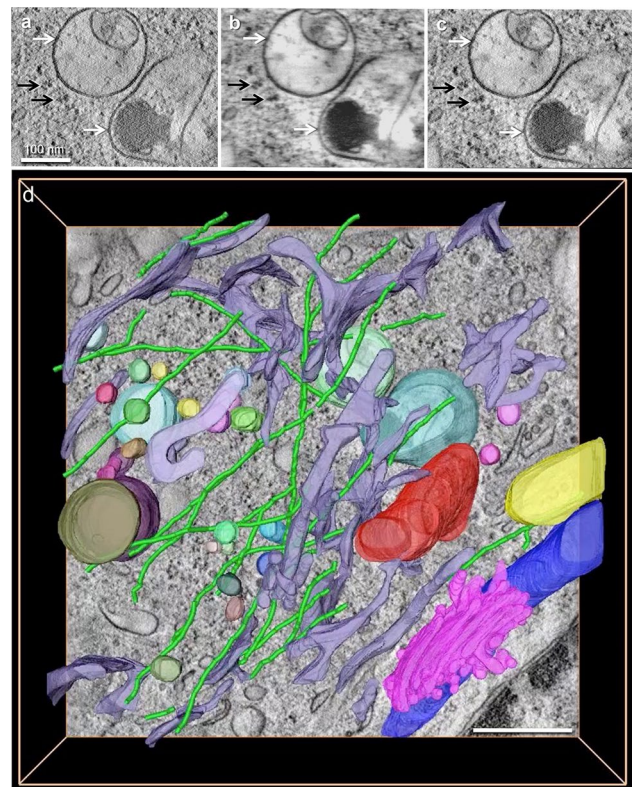
Fig. 6 Tomogram of the cytoplasm of a glioblastoma cell. **a** A portion of a virtual section reconstructed with the weighted back-projection (WBP) algorithm. Small details like the lipid bilayer (white arrows) are well resolved; bar 100 nm. **b** Reconstructed with the simultaneous iterative reconstruction technique (SIRT). The details are less well preserved, but the gray levels are less uniform than with WBP and different structures such as ribosomes (black arrows) occur darker than the rest of the cytosol, compared to what we are used to observe in conventional TEM. **c, d** Both signals are mixed, so the advantages of both approaches are combined. Color code for the segmentation: microtubules (green), Golgi apparatus (magenta), endoplasmic reticulum (purple), red and yellow mitochondria (red and yellow), vesicles (blue), tumor-specific autophagolysosomes (turquoise and umbra); bar 500 nm

Discussion

Technical limitations of STEM tomography

High-pressure freezing, freeze substitution, followed by STEM tomography is a powerful approach for structural studies in cell biology. Accordingly, the samples can be searched easily and rapidly, for an area of interest in the electron microscope. Afterwards the tilt series for the tomograms can be recorded. This is especially important for molecular biology research, when a large number of control experiments need to be analyzed.

When comparing the high-end Titan 300 kV with the more conventional JEOL 2100F 200-kV microscope, the Titan produces slightly better results, because in thick sections the upper part of the sections looks excellent with both
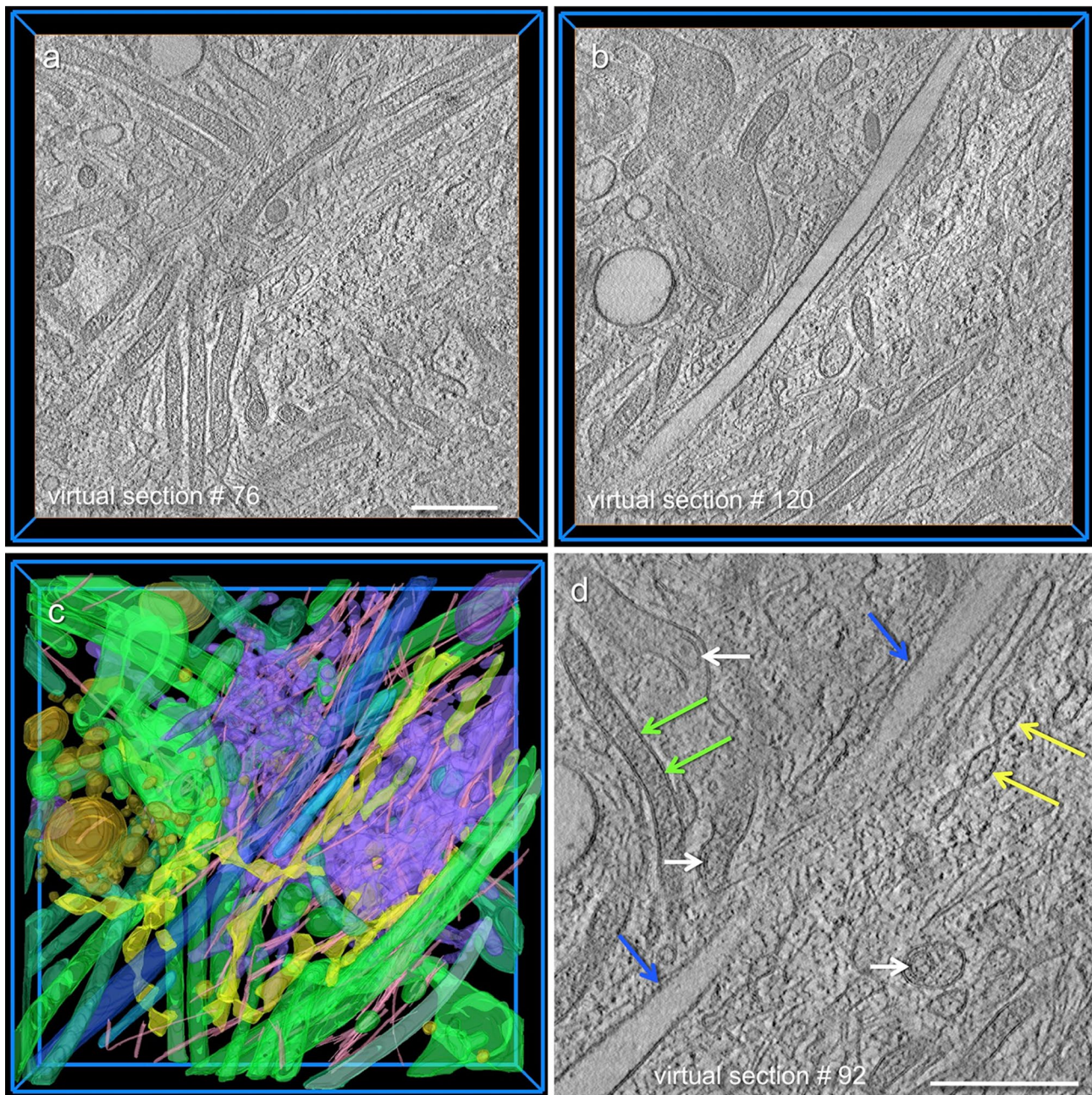
Fig. 7 Tomogram from the cytoplasm of a human M2 macrophage. Different tubules are omnipresent. **a** is a virtual section from the upper part of the tomogram, **b** from the lower part, **c** is a segmentation. Large empty tubules colored blue in the segmentation and labeled with blue arrows in the higher magnification image of the virtual section 92 (**d**). Densely filled tubules also contain membranes and membrane-derived fragments (white arrows) colored in green (green arrows in **d**). Chain-like tubules of variable diameters are labeled yellow. Conventional vesicles brown; microtubules red; endoplasmic reticulum purple; bars 500 nm

microscopes, whereas the bottom part of the tomogram is somewhat more blurred in the JEOL 2100F (Fig. 4). This is because of two reasons. Firstly, the mean free path of the electrons in the sample is shorter at 200 kV than at 300 kV. Therefore there is more scattering at 200 kV and, therefore more broadening of the primary beam. This widened beam then causes a blurred image in the depth of the sample.

The second effect is caused by the convergence angle of the primary beam. The convergence angle in the Titan is very small, due to the "parallel" beam alignment (Biskupek et al. 2010). The larger the convergence angle, the shorter is the depth of focus. We are currently addressing this issue by experiments aimed at quantification of these two effects on our instruments. First results indicate that both effects
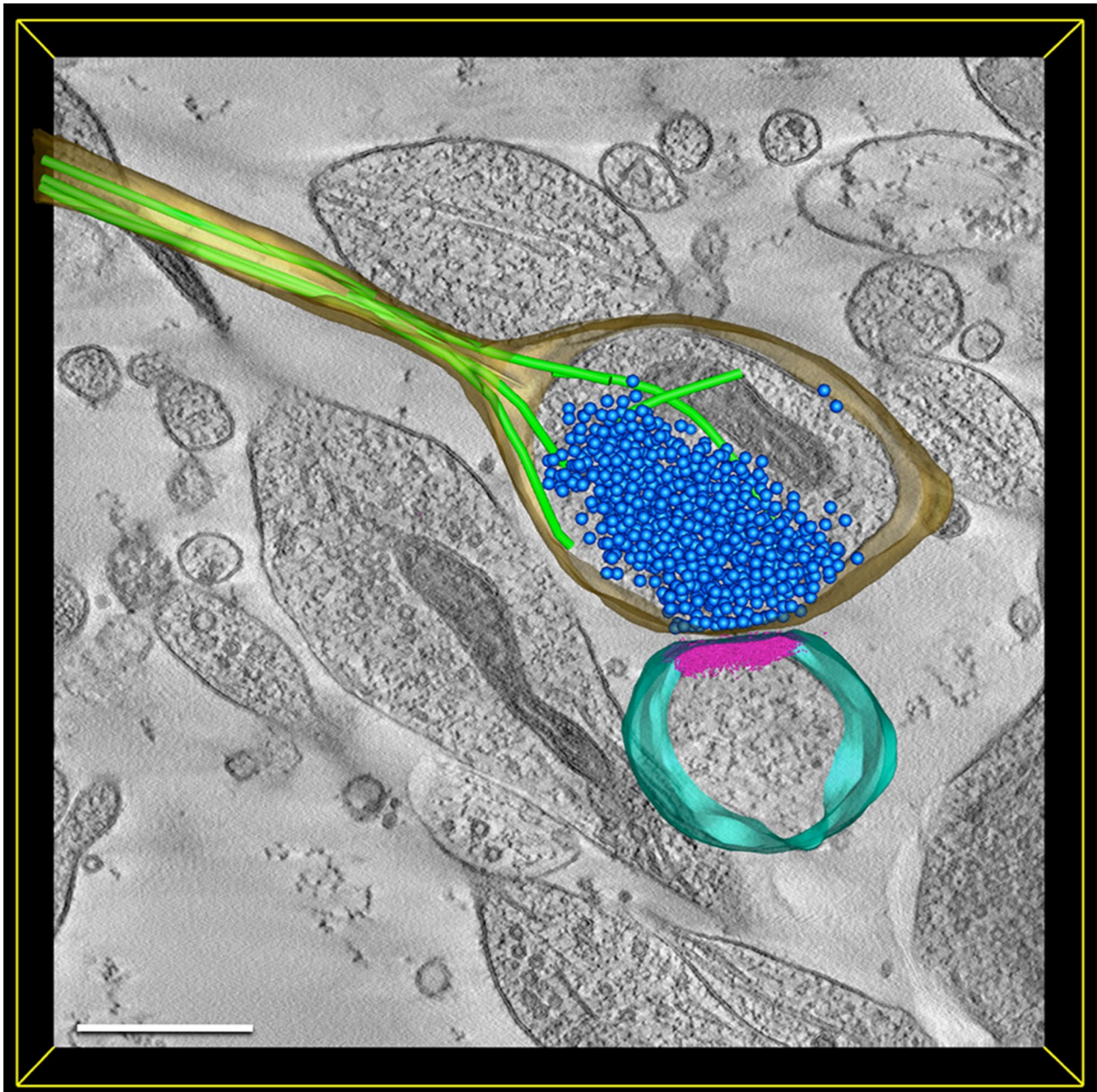
Fig. 8 A synapse from cultivated neuronal rat cells from embryonal hippocampal brain tissue. Color code: microtubules (light green), synaptic vesicles (blue), postsynaptic density area (magenta), pre-synaptic neuron (brown), due to its orientation, the postsynaptic site (turquoise) is only partially visible in the reconstructed section; bar 500 nm

contribute to the slightly better performance of the Titan 300-kV instrument. Figures 5, 6, 7 and 8, however, demonstrate that the JEOL 200-kV instrument also leads to excellent and very useful data sets.

Some technical challenges remain. The first is related to the observation that the tomograms are about 15–25% thinner than the settings in the ultramicrotome. We can imagine the following two reasons: shrinking of the sections when they are mounted and dried on the copper grid, and/or shrinking of the sample due to irradiation with the electron beam during acquisition of the tomograms. Since the amount of shrinking is quite reproducible and independent from the irradiation time, we guess that it is mainly caused by the drying process of the section on the grid. However, more investigations need to be done to fully explain this effect. The second technical aspect was whether

the bright-field or the dark-field signal should be used for tomography. Our results are in line with the earlier observation of Hohmann-Marriott et al. (2009). On thick sections the bright-field image gives better results, especially in the depth of the sample, where the dark field image is more blurred for geometrical reasons.

Applications of STEM tomography in life science

Figures 5, 6, 7 and 8 show applications of STEM tomography. In Fig. 5, filaments are winding around a branching mitochondrion. It would be impossible to observe this event in a 2D image (Sanders et al. 2018).

In Fig. 7, we found an extended tubular network system that resembles the structures described earlier as tubular lysosomal network or endolysosomal system (e.g., Klumperman and Raposo 2014). It looks very different from the spherical organelles commonly described as lysosomes in text books. We assume that this might partially be caused because tubules are more readily recognized in three-dimensional reconstructions; in two-dimensional images, a cross section of a tubule results in a circle or an ellipse and can be misinterpreted as a spherical vesicle. In the end, we consider STEM tomography as the method of choice to track such tubular networks, especially, since thick sections (up to 685 nm in this study) can be analyzed. This affords the opportunity to demonstrate a substantial portion of the network that is within a section. Moreover, the resolution remains to be adequate for resolution of the two layers of the lipid bilayer membrane. Using three-dimensional electron microscopy we recently described an endocytotic pathway in M2 macrophages that we called megapinocytosis (Bauer et al. 2016). We are currently working on a separate publication shedding light on this expanded tubular network and its connections with the megapinosomes (Bauer et al. in prep.).

Figure 8 shows a synapse. This structure is well suited to be investigated by STEM tomography because it is a structure that almost fully fits into an approximately 500-nm-thick section. In Fig. 8, however, a major part of the postsynaptic site is not in the section plane. Of course this limitation could be addressed by serial section-based STEM tomography.

STEM tomography compared with other approaches for three-dimensional electron microscopy

Scanning transmission electron microscopic tomography of high-pressure frozen and freeze-substituted samples is the method of choice when portions of a cell need to be investigated in three dimensions with a resolution in the order of a few nm on X and Y. Since on freeze substituted samples we do not image the biological structure directly, but the attached heavy metal stain, we will definitely never reach atomic resolution with this approach. Therefore resolution-wise our approach cannot compete with cryo-TEM, where contrast is formed by the biological material; it has, however the advantage that our samples are very well protected against beam damage. When looking at a membrane with a thickness of roughly 5 nm, three structures, a dark line, a bright line, and another dark line can be distinguished, usually. These lines correspond to the heads (dark) and the tails (bright) of the bilayer. We therefore estimate that the resolution of the approach ranges between 2 nm and 3 nm in X and Y. As can be seen in Figs. 1 and 3, the resolution is slightly poorer in Z. This is due to the "missing wedge effect" (Baumeister 2004), caused by the fact that we cannot tilt the sample to 90° but only to about 72°.

In an earlier manuscript, we compared STEM tomography with FIB-SEM tomography (Villinger et al. 2012). When setting the appropriate conditions for imaging (5 kV accelerating voltage and secondary electron imaging), we also succeeded to resolve the three areas of the lipid bilayer. The resolution in Z is limited in FIB-SEM due to the amount of sample which has been removed stepwise by the FIB (focused ion beam). If this amount is very small, e.g., 5 nm, many images are required to go through a thick object (e.g., 1000 images for 5 μm) and the process will take a long time. So, to summarize, with STEM tomography we can rapidly search for a good area on the sample. We then can take several datasets from the same area, e.g., at different magnifications, if necessary. With FIB-SEM, searching is more difficult since it is done in the surface SEM mode where no details of the inner part of the cell are visible. After data collection with FIB-SEM the area is destroyed and we cannot reimage the same area on the sample. On the other hand, with FIB-SEM we can analyze thicker areas. With STEM sample, thickness is limited to about 1 μm for the reasons explained above.

It is certainly worth mentioning in this context that cryo-STEM tomography, the analysis of frozen hydrated samples with STEM, is a new, very promising approach. It also allows for investigation of thicker samples than used in cryo-TEM. It has, however, to be done under low-dose conditions, since frozen hydrated samples are highly beam sensitive (Wolf et al. 2014, 2017).

GmbH for his abundance of patience at the phone, answering our amateurish questions, and for always getting our STEM system back to work. We finally thank David Mastronarde and his team for developing the IMOD software and making it freely available for everybody and for the counseling via the IMOD list.

References

Aoyama K, Takagi T, Hirase A, Miyazawa A (2008) STEM tomography for thick biological specimens. Ultramicroscopy 109:70–80

Bauer A, Subramanian N, Villinger C, Frascaroli G, Mertens T, Walther P (2016) Megapinocytosis: a novel endocytic pathway. Histochem Cell Biol 145:617–627

Bauer A, Frascaroli G, Walther P (2017) STEM tomography unveils lysosomal tubular networks in macrophages. In: Laue M (ed) Microscopy conference 2017 (MC 2017)—proceedings LS2. P005, Regensburg

Baumeister W (2004) Mapping molecular landscapes inside cells. Biol Chem 385:865–872

Biskupek J, Leschner J, Walther P, Kaiser U (2010) Optimization of STEM tomography acquisition—a comparison of convergent beam and parallel beam STEM tomography. Ultramicroscopy 110:1231–1237

Catanese A, Garrido D, Walther P, Roselli F, Boeckers TM (2018) Nutrient limitation affects presynaptic structures through dissociable Bassoon autophagic degradation and impaired vesicle release. J Cereb Blood Flow Metab. https://doi.org/10.1177/0271678X18786356

Daems WT, Wisse E (1966) Shape and attachment of the cristae mitochondriales in mouse hepatic cell mitochondria. J Ultrastruct Res 16:123–140

Giehl K, Bachem M, Beil M, Böhm BO, Ellenrieder V, Fulda S, Gress TM, Holzmann K, Kestler HA, Kornmann M, Menke A, Möller P, Oswald F, Schmid RM, Schmidt V, Schirmbeck R, Seufferlein T, von Wichert G, Wagner M, Walther P, Wirth T, Adler G (2011) Inflammation, regeneration, and transformation in the pancreas: results of the Collaborative Research Center 518 (SFB 518) at the University of Ulm. Pancreas 40(4):489–502

Han S, Kollmer M, Markx D, Claus S, Walther P, Fändrich M (2017) Amyloid plaque structure and cell surface interactions of β-amyloid fibrils revealed by electron tomography. Sci Rep 7:43577

Hochapfel F, Denk L, Maaßen C, Zaytseva Y, Rachel R, Witzgall R, Krahn MP (2018) Electron microscopy of Drosophila garland cell nephrocytes: optimal preparation, immunostaining and STEM tomography. J Cell Biochem. https://doi.org/10.1002/jcb.26702

Hohmann-Marriott MF, Sousa AA, Azari AA, Glushakova S, Zhang G, Zimmerberg J, Leapman RD (2009) Nanoscale 3D cellular imaging by axial scanning transmission electron tomography. Nat Methods 6:729–731

Höhn K, Sailer M, Wang L, Lorenz L, Schneider EM, Walther P (2011) Preparation of cryofixed cells for improved 3D ultrastructure with scanning transmission electron tomography. Histochem Cell Biol 135:1–9

Hoppe W, Gassmann J, Hunsmann N, Schramm HJ, Sturm M (1974) Three-dimensional reconstruction of individual negatively stained yeast fatty-acid synthetase molecules from tilt series in the electron microscope. Z Physiol Chem 355:1483–1487

Klumperman J, Raposo G (2014) The complex ultrastructure of the endolysosomal system. Cold Spring Harb Perspect Biol 6:a016857

Knoll G, Brdiczka D (1983) Changes in freeze-fractured mitochondrial membranes correlated to their energetic state dynamic interactions of the boundary membranes. Biochim Biophys Acta 733:102–110

Kollmer M, Meinhardt K, Haupt C, Liberta F, Wulff M, Linder J, Handl L, Heinrich L, Loos C, Schmidt M, Syrovets T, Simmet T, Westermark P, Westermark GT, Horn U, Schmidt V, Walther P, Fändrich M (2016) Electron tomography reveals the fibril structure and lipid interactions in amyloid deposits. Proc Natl Acad Sci USA 113:5604–5609

Kremer JR, Mastronarde DN, McIntosh JR (1996) Computer visualization of three-dimensional image data using IMOD. J Struct Biol 116:71–76

Liu W, Naydenov B, Chakrabortty S, Wünsch B, Hübner K, Ritz S, Cölfen H, Barth H, Koynov K, Qi H, Leiter R, Reuter R, Wrachtrup J, Boldt F, Scheuer J, Kaiser U, Sison M, Lasser T, Tinnefeld P, Jelezko F, Walther P, Wu Y, Weil T (2016) Fluorescent nanodiamond-gold hybrid particles for multimodal optical and electron microscopy cellular imaging. Nano Lett 16:6236–6244

McBride EL, Rao A, Zhang G, Hoyne JD, Calco GN, Kuo BC, He Q, Prince AA, Pokrovskaya ID, Storrie B, Sousa AA, Aronova MA, Leapman RD (2018) Comparison of 3D cellular imaging techniques based on scanned electron probes: Serial block face SEM vs. axial bright-field STEM tomography. J Struct Biol 202:216–228

Müller SA, Engel A (2001) Structure and mass analysis by scanning transmission electron microscopy. Micron 32:21–31

Nafeey S, Martin I, Felder T, Walther P, Felder E (2016) Branching of keratin intermediate filaments. J Struct Biol 194:415–422

Sanders P, Walther P, Moepps M, Hinz M, Mostafa H, Schaefer P, Pala A, Wirtz CR, Georgieff M, Schneider EM (2018) Mitophagy-related cell death mediated by vacquinol-1 and TRPM7 blockade in glioblastoma IV. In: For "Glioma—contemporary diagnostic and therapeutic approaches". InTechOpen (in press)

Schauflinger M, Fischer D, Schreiber A, Chevillotte M, Walther P, Mertens T, von Einem J (2011) The tegument protein UL71 of human cytomegalovirus is involved in late envelopment and affects multivesicular bodies. J Virol 85: 3821–3832

Schauflinger M, Villinger C, Mertens T, Walther P, von Einem J (2013) Analysis of human cytomegalovirus secondary envelopment by advanced electron microscopy. Cell Microbiol 15:305–314

Villinger C, Gregorius H, Kranz Ch, Höhn K, Münzberg C, von Wichert G, Mizaikoff B, Wanner G, Walther P (2012) FIB/SEM-tomography with TEM-like resolution for 3D imaging of high pressure frozen cells. Histochem Cell Biol 138:549–556

Villinger C, Schauflinger M, Gregorius H, Kranz C, Höhn K, Nafeey S, Walther P (2014) Three-dimensional imaging of adherent cells using FIB/SEM and STEM. Methods Mol Biol 1117:617–638

Walther P, Ziegler A (2002) Freeze substitution of high-pressure frozen samples: the visibility of biological membranes is improved when the substitution medium contains water. J Microsc 208:3–10

Walther P, Wang L, Ließem S, Frascaroli G (2010) Viral infection of cells in culture—approaches for electron microscopy. Methods Cell Biol 96:603–618

Wolf SG, Houben L, Elbaum M (2014) Cryo-scanning transmission electron tomography of vitrified cells. Nat Methods 11:423–428

Wolf SG, Mutsafi Y, Dadosh T, Ilani T, Lansky Z, Horowitz B, Rubin S, Elbaum M, Fass D (2017) 3D visualization of mitochondrial solid-phase calcium stores in whole cells. Elife 6:e29929

Yakushevska AE, Lebbink MN, Geerts WJ, Spek L, van Donselaar EG, Jansen KA, Humbel BM, Post JA, Verkleij AJ, Koster AJ (2007) STEM tomography in cell biology. J Struct Biol 159:381–391

Yin X, Ziegler A, Kelm K, Hoffmann R, Watermeyer P, Alexa P, Villinger C, Rupp U, Schlüter L, Reusch TBH, Griesshaber E, Walther P, Schmahl WW (2018) Formation and mosaicity of coccolith segment calcite of the marine algae Emiliania huxleyi. J Phycol 54:85–104

Zierold K, Steinbrecht A (1987) Cryofixation of diffusible elements in cells and tissues for electron probe microanalysis. In: Steinbrecht RA, Zierold K (eds) Cryotechniques in biological electron microscopy. Springer, Heidelberg, pp 3–34